minerals

MDPI

Article

Ion and Particle Size Effects on the Surface Reactivity of Anatase Nanoparticle–Aqueous Electrolyte Interfaces: Experimental, Density Functional Theory, and Surface Complexation Modeling Studies

Moira K. Ridley [1,*], Michael L. Machesky [2] and James D. Kubicki [3]

[1] Department of Geosciences, Texas Tech University, Lubbock, TX 79409, USA
[2] Illinois State Water Survey, University of Illinois, 1506 Coral Cove Drive, Champaign, IL 61821, USA; machesky@illinois.edu
[3] Department of Earth, Environmental & Resource Sciences, The University of Texas at El Paso, El Paso, TX 79968, USA; jdkubicki@utep.edu
* Correspondence: moira.ridley@ttu.edu

Abstract: At the nanoscale, particle size affects the surface reactivity of anatase–water interfaces. Here, we investigate the effect of electrolyte media and particle size on the primary charging behavior of anatase nanoparticles. Macroscopic experiments, potentiometric titrations, were used to quantitatively evaluate surface charge of a suite of monodisperse nanometer sized (4, 20, and 40 nm) anatase samples in five aqueous electrolyte solutions. The electrolyte media included alkaline chloride solutions (LiCl, NaCl, KCl, and RCl) and Na-Trifluoromethanesulfonate (NaTr). Titrations were completed at 25 °C, as a function of pH (3–11) and ionic strength (from 0.005 to 0.3 m). At the molecular scale, density functional theory (DFT) simulations were used to evaluate the most stable cation surface species on the predominant (101) anatase surface. In all electrolyte media, primary charging increased with increasing particle size. At high ionic strength, the development of negative surface charge followed reverse lyotropic behavior: charge density increased in the order RbCl < KCl < NaCl < LiCl. Positive surface charge was greater in NaCl than in NaTr media. From the DFT simulations, all cations formed inner-sphere surface species, but the most stable coordination geometry varied. The specific inner-sphere adsorption geometries are dependent on the ionic radius. The experimental data were described using surface complexation modeling (SCM), constrained by the DFT results. The SCM used the charge distribution (CD) and multisite (MUSIC) models, with a two-layer (inner- and outer-Helmholtz planes) description of the electric double layer. Subtle charging differences between the smallest and larger anatase particles were the same in each electrolyte media. These results further our understanding of solid–aqueous solution interface reactivity of nanoparticles.

Keywords: anatase; nanoparticle; lyotropic series; surface complexation modeling; mineral–water interfaces

Citation: Ridley, M.K.; Machesky, M.L.; Kubicki, J.D. Ion and Particle Size Effects on the Surface Reactivity of Anatase Nanoparticle–Aqueous Electrolyte Interfaces: Experimental, Density Functional Theory, and Surface Complexation Modeling Studies. *Minerals* **2022**, *12*, 907. https://doi.org/10.3390/min12070907

Academic Editors: Katharina Müller and Norbert Jordan

Received: 4 April 2022
Accepted: 7 July 2022
Published: 20 July 2022

1. Introduction

The macroscopic phenomenon of surface charge at mineral–water interfaces is well established [1–3]. Equally recognized are the distinct trends in the development of surface charge that follow ion-specific cation and anion trends, often termed as lyotropic or Hofmeister series. Of importance to the environmental sciences is the development of surface charge arising from interactions between alkali and alkali-earth cations, specifically alkali-chlorides, and mineral surfaces. Trends in the charging behavior of silica and rutile along the alkali-chloride lyotropic series have been studied most [1,4–12]. On silica, negative charge development follows "regular" lyotropic behavior, with charge density increasing with cation crystallographic radius in the order LiCl < NaCl < KCl < CsCl [1,4–9]. However, rutile exhibits the reverse trend; negative charge density increases

from RbCl < KCl < NaCl < LiCl [9–12]. Flow microcalorimetry measurements investigating the heats of adsorption and exchange of the alkali cations at silica–and rutile–water interfaces also show regular and reverse lyotropic series, respectively [5,12]. The interaction between alumina (sapphire, α–Al_2O_3) surfaces and cations, in chloride systems, is more complex [13]. Electrokinetic experiments conducted on the (001) and (012) surfaces (i.e., c- and r-plane, respectively) of alumina have shown different behavior. As for rutile, the alumina (012) surface displayed cation specificity following reverse lyotropic behavior (i.e., $Li^+ > Na^+ > K^+ > Rb^+ > Cs^+$). No cation specific effects were noted for the (001) surface, in cation-chloride media.

The mechanisms behind the development of surface charge, specifically negative charge, for a given metal–oxide in 1:1 alkali-ion salt solutions have yet to be fully resolved. However, experimental and computational results collectively suggest that electrostatic interactions that occur directly between the alkali cation and mineral surface may be the most important. There appears to be a correlation between the structural and chemical properties of the surface—dielectric constants and polarizability of the solid [14], and surface site acidity—and the loss of primary hydration water molecules (desolvation) of the alkali cations that directly influences the development of surface charge.

Electrostatic interactions between mineral surfaces and ions necessitate restructuring of interfacial and solvation water molecules. Interactions that favor the loss of hydration water molecules from cations, allow ions to move close to the surface, forming inner-sphere surface complexes that effectively screen the surface from bulk solution. Cations that retain solvation water molecules as they approach a mineral surface will form longer-range electrostatic interactions, outer-sphere complexes, resulting in a lower surface charge density (i.e., proton induced surface charge, determined from potentiometric experiments). Some studies have related the loss of hydration water from mono- and divalent cations to the change in hydration entropy in the interface [4], and enthalpy of adsorption [12]. For rutile, a high dielectric constant solid [14], X-ray synchrotron measurements, vibrational sum frequency spectroscopy (VSFS), and molecular-scale simulations show that alkali cations form inner-sphere complexes with the (110) surface [9,10,14]. And, the synchrotron and simulation studies show that Na^+ ions adsorbed more closely to the rutile surface than K^+ and Rb^+ ions do. The adsorption height of monovalent cations above the rutile surface follows the bare cation radius, $Na^+ < K^+ < Rb^+$, and correlates with an increase in surface charge density observed in potentiometric titrations [10,15]. Consequently, by simply changing the specific electrolyte ions in aqueous media the microscopic structure of the mineral–water interfacial domain, known as the electric double layer (EDL), changes. Changes within the EDL structure regulate chemical reactivity of surfaces, which affects, for example, adsorption, catalysis, and biological processes [1].

Surface charge and EDL structure of nanosized particles is of special interest because surface charge underlies the inherent differences in chemical behavior of nanometer versus macroscopic particles for a given material. It is well established that the intrinsic structural and chemical properties of nanoparticles control their aggregation and dispersion, biomolecule and protein interactions, and toxicity —all processes mediated by surface charge at the solid–water interface. Previous work has systematically evaluated the assumption that surface charge varies as a function of particle size [16–23]. The results of these studies are ambiguous. Our work on anatase, the stable TiO_2 polymorph at the nanometer scale, showed that in NaCl media, the pH of zero net proton charge (pH_{znpc}) for 4 and 20 nm sized powders was higher than for a 40 nm size sample (6.42 and 6.22, respectively). Additionally, surface charge density increased with particle size in the order 4 < 20 < 40 nm [24–27]. We rationalized the observed differences as the monovalent electrolyte cations being able to screen the larger sized particles more effectively from the bulk solution than was possible for the smaller particles. This reasoning followed from the accepted premise that macroscopically observable surface charge trends are regulated by the distance of closest approach of ions to a mineral surface, which is affected by particle

morphology (i.e., spherical versus platy) [21,28]. As outlined below, the 20 and 40 nm sized particles are spherical, whereas the 4 nm sized particles are platy or lath-like.

Two questions that arise from our nanoparticle anatase–NaCl media studies, is whether the observed trends extend to other electrolyte media. Additionally, whether the surface charging behavior of different sized nanoparticle anatase powders also follow the reverse monovalent cation lyotropic series, as that observed for larger anatase particles and rutile [29,30]. There are key differences between the two TiO_2 polymorphs: anatase has a more open structure, and is a lower dielectric constant solid (bulk ε = 18.6 and 121 for anatase and rutile, respectively) [14]; the latter difference may be particularly significant for the desolvation of electrolyte cations. Our objective in this study was to systematically address these two questions. We quantitatively evaluated the surface charge behavior of nanoparticle anatase in KCl, RbCl, LiCl, and Na-Trifluoromethanesulfonate (NaTr) media. We performed potentiometric titrations, with the three monodisperse anatase samples (4, 20, and 40 nm sized particles) used in the NaCl media study [26]. Our aim was to do more than just evaluate macroscopic trends in the behavior of anatase nanoparticles in various electrolyte media, but also to utilize microscopic detail to rationalize observable differences. Molecular-scale information was obtained from molecular dynamics–density functional theory (MD-DFT) simulations for the adsorption of Na^+, K^+, Rb^+, Li^+, and Cl^- ions on the anatase (101) surface.

2. Materials and Methods

2.1. Anatase

A detailed description of the three anatase powders used in this study has been presented previously [20,22,23]. Here, we provide only a brief overview. The three samples were monodispersed powders (i.e., particle size was uniform, with minimal variation), with average particle sizes of approximately 4, 20 and 40 nm. The average range in particle size, of the three samples, was 3.6–4.6, 18–22, and 35–46 nm (see [26] for an extensive description of the physical characteristics of the 4 nm sample). The 4 and 20 nm sized powders were obtained from Ishihara Techno Corp. (Osaka, Japan); the third sample was obtained from Altair Nanomaterials, Inc. (Reno, NV, USA). Before use, all samples were washed and characterized extensively [24,26]. Electron microscopy analysis, specifically aberration corrected electron microscopy (ACEM), enabled identification of the predominant crystal faces. Imaging showed that the (101) surface plane was dominant on all samples [26]. The crystal faces were sub-equant; the particles were thin, slightly wedge-shaped, and tapered toward the edge. The surfaces were relatively smooth. Brunauer-Emmett-Teller (BET) N_2-adsorption was used to measure the surface area of the washed samples. Measured surface area values are within 15% of calculated values assuming spherical particles, the difference reflects the lath-like particle shape (Table 1).

2.2. Experimental

The surface titration procedure developed specifically for nanoparticles, by Ridley et al. [24], was followed throughout this study. The procedure ensures that the reactivity of the entire surface area of the primary crystallites is accessed, and not just the surface of closely packed aggregates. For completeness, an overview of the titration procedure is presented here. All titrations were performed at 25 °C (±0.1 °C), utilized a Mettler T90 autotitrator, a semimicro combination glass electrode, and a mechanical stirrer. Each titration was performed using sufficient anatase powder to provide approximately 12–14 m^2 of surface area (Table 1). The anatase powder was suspended in 16–20 g of acid dispersion solution, the powder was dispersed using a high-intensity (750 W) ultrasonicator with an immersible titanium horn. The suspension (i.e., dispersed anatase powder and test solution) was transferred to a titration cell, suspension mass was adjusted to 40 g, the cell was sealed, purged with argon, placed in a water bath, and allowed to equilibrate at 25 °C for 1 h. After calibrating the electrode at the appropriate ionic strength, the titrations proceeded by the addition of 20–30 aliquots of base titrant. Initial equilibration

and throughout the titrations, equilibration of the anatase suspension was assumed when the potential drift was <0.05 mV/min. Titrations were completed in approximately 4 h, which was sufficiently rapid to limit the growth and aggregation, or dissolution of the nanoparticles [24]. The stable potential, short experimental time, and low solubility of nanoparticle anatase (under the experimental solution conditions) suggested that dissolution, if any, was minimal [12,31,32]. Each titration yielded a single set of acid-to-base titration data. Data reduction followed standard procedures described in detail by Ridley et al. [24]. Data reduction included calculating activity coefficients, using a combined extended Debye-Hückel–Pitzer formulation [33]. The calculated activity coefficients were used in the SCM efforts described below.

Table 1. Physical characteristics, experimental pH_{znpc} values, MUSIC model parameters [1], and predicted protonation constants [2] for the three anatase samples [3].

Parameter	4 nm	20 nm	40 nm
N_2-BET surface area (m^2/g)	300 ± 0.4	66.4 ± 0.3	44.0 ± 0.3
Approximate mass of anatase per titration (g) [4]	0.04	0.22	0.32
pH_{znpc}	6.42 ± 0.16	6.42 ± 0.43	6.22 ± 0.16
log K_{H1}	6.82	6.82	6.62
log K_{H2}	5.99	5.99	5.75
Fractional charge on ≡TiOH	−0.31	−0.31	−0.31
Fractional charge on $\equiv Ti_2O$	−0.68	−0.68	−0.67
Ti–O bond length $\equiv TiOH^{-0.3}$	1.94 Å	1.94 Å	1.93 Å
Ti–O bond length $\equiv Ti_2O^{-0.7}$	1.95 Å	1.95 Å	1.95 Å

[1] In the MUSIC model calculations, Ro = 1.796. Surface complexation modeling is discussed below. [2] The protonation reactions for log K_{H1} and log K_{H2} are presented below. Log K values reflect infinite dilution. [3] The pH_{znpc} value for the 4 nm sample has an offset of −0.062 µmols H^+/m^2, which was applied as a correction to all titration data of the 4 nm sample [26]. [4] The total mass of the suspension was 40 g (see text).

All experimental solutions were prepared from reagent-grade chemicals and deionized water. The dispersion solutions contained sufficient HCl to give a starting composition generally close to 0.002 m H^+ (where m indicates aqueous concentration in units of molality, moles of solute per kilogram of water). The base titrant solutions comprised NaOH (approximately 0.025 m OH^-), and the appropriate electrolyte. Titrations were performed over a range of ionic strengths from 0.005 to 0.3 m. A complete set of titration solutions (i.e., electrode calibration, dispersion, and titrant solutions) was prepared at each ionic strength, for each of the five ionic media: NaCl, KCl, RbCl, LiCl, and NaTr. Titrations were performed at five ionic strengths in NaCl media (0.005, 0.01, 0.03, 0.06, and 0.3 m), three in KCl (0.03, 0.06, and 0.3 m), and two for RbCl, LiCl, and NaTr (0.03, and 0.3 m). The starting pH of the 0.005 and 0.01 m ionic strength NaCl media titrations was increased slightly, close to 0.001 m H^+ (Figure 1) [26]. For the 0.3 m ionic strength KCl, RbCl, and LiCl titrations, the contribution of Na^+ ions to ionic strength was less than 1%, whereas the Cl salts comprised less than 9% Na^+ ions in the 0.03 m suspensions. Similarly, for the NaTr titrations, the Cl salts contributed less than 1 or 7% Cl^- ions to the 0.3 and 0.03 m suspensions, respectively.

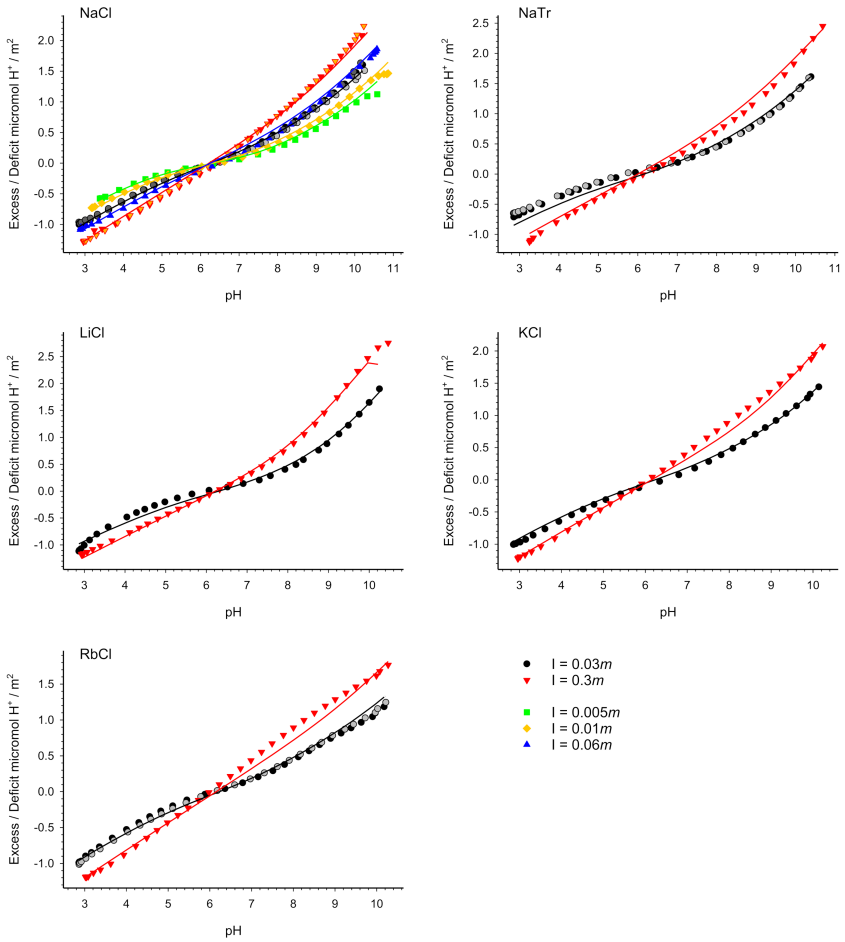

Figure 1. Relative proton adsorption or desorption on the 4 nm sized anatase sample in each electrolyte media. The symbols represent experimental data, and lines represent the SCM best fits. The model parameters are defined in the text and are given in Tables 1 and 2.

2.3. Molecular Modeling

Relative energies and possible structures for the interaction of Na^+, K^+, Rb^+, Li^+, and Cl^- ions on the (101) anatase surface were evaluated using MD-DFT simulations. For the simulation studies, we constructed the (101) anatase surface using the Surface Builder module of Materials Studio version 6.0 (Biovia, San Diego, CA). The Ti atom valences on the anatase surface were satisfied by bonding H_2O molecules to the 5-fold Ti atoms. Each simulation system comprised the anatase slab ($Ti_{48}O_{96}$), 62 H_2O molecules, and a 20 Å vacuum gap; the resulting dimensions of the simulation cells were 15.224 Å × 10.4516 Å × 30.0 Å. For the four chloride electrolytes, simulations were performed by adding a Cl^- ion and the relevant cation to the model systems. The small number of included water molecules was not intended to represent bulk water; rather the systems were designed to allow minimal solvation of the surface and adsorbed ions. For each electrolyte, the initial position and coordination geometry of the cations was varied. A representative example of the complete simulation system, for RbCl, is shown in Figure S1 of the Supplementary Material.

The MD-DFT calculations were performed using the Vienna ab initio simulation package (VASP) [34,35]. Projector-augmented planewave pseudopotentials were used with the PBE gradient-corrected exchange correlation functional for the three-dimensional periodic calculations. One k-point samplings and an energy cutoff of 500 eV were used. Initially, each system was relaxed until the energy gradient was less than 0.02 eV/Å. The MD simulations were performed with 0.5 fs times steps, for 2 ps at 300 K, using the Nosé thermostat (SMASS = 0.028) [36,37]. The short duration of the MD simulations allowed all atoms to relax away from high energy configurations; minimal energy configurations were

not expected. For each composition (i.e., LiCl, NaCl, KCl, and RbCl), the energy changes were solely due to the various configurations (e.g., bidentate, tetradentate, outer-sphere) modeled; hence, energy differences can be directly ascribed to the relative stability of the bonding arrangements of the adsorbed ions. The calculated energy differences were on the order of 100 kJ/mol; therefore, one can infer that the lower energy configurations will be thermodynamically stable because entropy differences are not expected to be more than ~20 kJ/mol due to loss of H_2O from the coordination shell (i.e., desolvation) [38]. The relative energy differences allow us only to infer the coordination geometry of the most likely adsorption complexes, and thus constrain surface complexation modeling efforts.

2.4. Surface Complexation Modeling

The surface charge data from the extensive suite of titrations conducted in NaCl media were used to determine the pH of zero net proton charge for anatase, and to estimate protonation constants for the surface functional groups that exist on the (101) anatase surface (Table 1) [24,26]. For completeness, we include a summary. The titration curves for the 20 and 40 nm sized samples intersected tightly at pH values close to the zero proton condition; therefore, the common intersection point pH values were equated with the pH_{znpc} values (Table 1). The 4 nm sized sample had a tight common intersection point at a pH of 6.42; however, this value was slightly offset from the zero proton condition (-0.062 μmols H^+/m^2). The small offset correction has been applied to all subsequent titration results for the 4 nm sized sample [26,27]. A shift in pH_{znpc} values, towards higher pH values, with decreasing particle size has been observed for other metal–oxide phases (e.g., maghemite, γ-Fe_2O_3 [20], see additional references in [26]). Error estimates for the pH_{znpc} values included in Table 1 reflect the maximum spread over all replicate titration data.

The (101) surface comprises two independent surface sites: 2-fold coordinated (bridged, $\equiv Ti_2O$) surface hydroxyls, and 5-fold coordinated Ti atoms (terminal, $\equiv$TiOH). The two sites are present in a 1:1 ratio, with a site density, N_S, of 10.3 sites/nm^2 (17.2 μmol/m^2). For bulk anatase, the average Ti–O bond lengths of the bridging surface groups are 1.95 Å, whereas the Ti–O bond length of the terminal group is slightly shorter, 1.94 Å [39,40]. Protonation constants were calculated following the MUSIC model framework of Hiemstra and van Riemsdijk [40,41], which include small adjustments to the surface bond lengths [26]. Changes of surface Ti–O bond lengths of anatase nanoparticles has been observed from DFT simulation studies [42–44]. All MUSIC model parameters and predicted protonation constants from Ridley et al. [26] were used in the present study, and are given in Table 1. The protonation reactions are represented by

$$\equiv \mathrm{TiOH}^{-0.3} + \mathrm{H}^+ \rightleftharpoons \equiv \mathrm{TiOH}_2^{+0.7} \rightarrow K_{\mathrm{H1}} \quad (1)$$

$$\equiv \mathrm{Ti_2O}^{-0.7} + \mathrm{H}^+ \rightleftharpoons \equiv \mathrm{Ti_2OH}^{+0.3} \rightarrow K_{\mathrm{H2}} \quad (2)$$

Surface complexation modeling was performed to describe and rationalize the potentiometric titration results for the three anatase samples in the five electrolyte media. The model fits were determined using custom Mathematica notebooks, and the fractional charges shown in Equations (1) and (2) were used throughout. The previously fitted NaCl media titration data were refitted here [26,27]. The SCM fits explicitly incorporated the DFT simulation results. Best-fit parameter values and model selection criterion (MSC) values were estimated using the Mathematica notebooks. The MSC value is a normalized inverse form of the Akaike Information Criterion [45]. It is a measure of the goodness of fit of the model, with larger values signifying better fits.

3. Results

3.1. Proton Adsorption Titrations

Figure 1 shows net proton adsorption curves (expressed as excess/deficit μmols H^+/m^2, calculated from H^+ mass balance) for the 4 nm sized anatase powder in each electrolyte medium. The net proton adsorption curves for the 20 and 40 nm diameter

anatase samples were comparable. In all electrolytes and for all anatase samples, standard deviation of the μmols H^+/m^2 values were determined from replicate titration data, with one standard deviation being smaller than the data symbols shown in Figure 1. For reference, all ionic strength data (from 0.005 to 0.3 m) are shown for the NaCl media. As is typical, the slope of the titration curves steepened with increasing ionic strength, and the titration isotherms exhibit a common intersection point that corresponds closely to zero μmols H^+/m^2. In this work, as described previously [26] and above (Section 2.4), the pH_{znpc} values were obtained from the extensive data set in NaCl media (Table 1).

The effect of particle size on the proton adsorption curves is shown in Figure 2, for titrations at 0.3 m ionic strength. The data are presented relative to the respective pH_{znpc} values of the three anatase samples (i.e., pH_{znpc}-pH), thus allowing for a direct comparison of the proton adsorption curves. In NaCl, NaTr, and LiCl media, the slope of the titration curves increases with increasing particle size above and below the pH_{znpc} value. In KCl and RbCl media, the 20 and 40 nm diameter particles have near identical slopes, whereas the 4 nm sized particles exhibit shallower curves. We also noted a small shift in the apparent pH_{znpc} value (0.1–0.2 pH units), towards lower pH values, for all particle sizes in KCl and RbCl media. The same trends were observed at all ionic strengths. However, different size-dependent behavior has been reported for other metal–oxide phases (e.g., goethite); specifically, for spherical particles smaller than 10 nm [16].

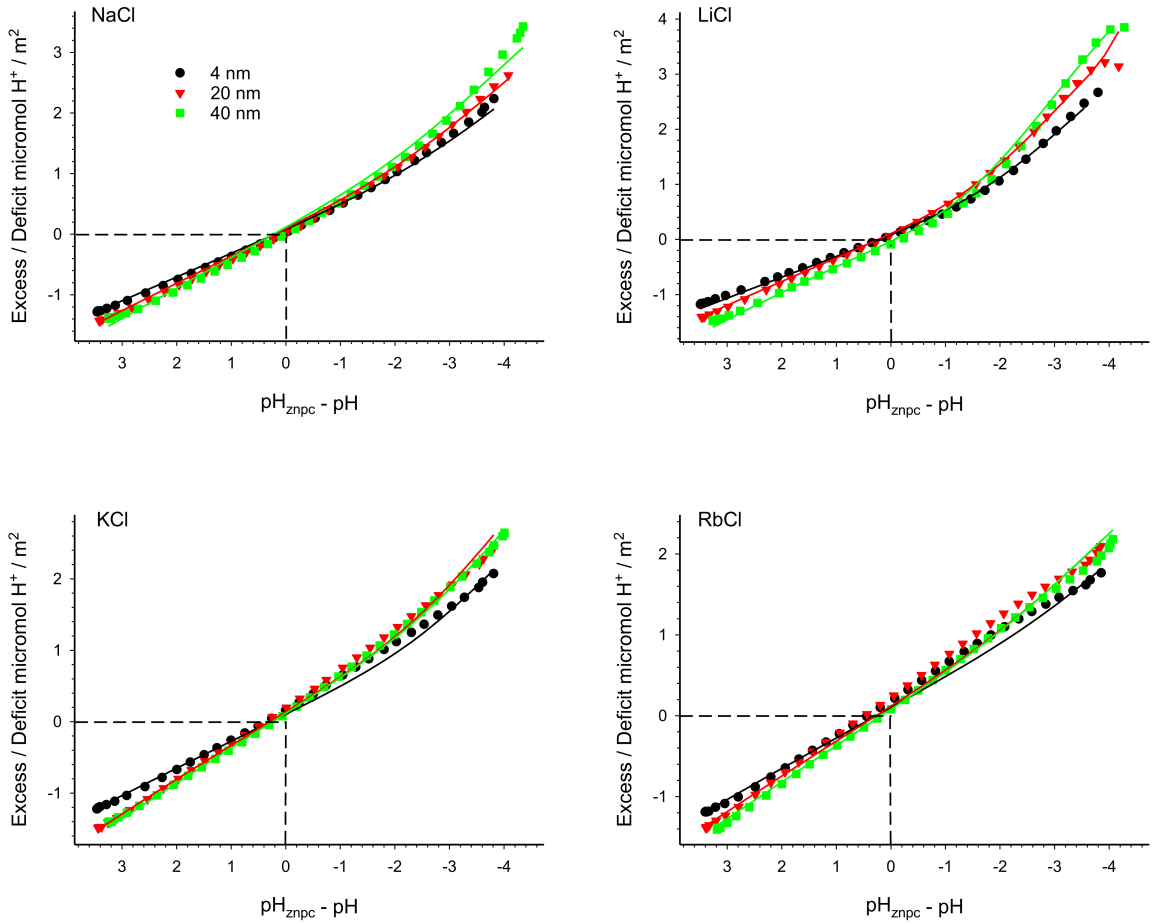

Figure 2. Titration data showing the effect of particle size on the relative proton adsorption or desorption as a function of pH_{znpc}-pH. Data are presented for titrations at an ionic strength of 0.3 m, in NaCl, LiCl, KCl, and RbCl media. The symbols represent experimental data, and lines represent the SCM best fits.

The net proton charge curves in the different cation-Cl electrolyte media were almost identical at low ionic strength (Figure 3) for the 4 nm sized particles. The only exception to this trend was Rb^+; above pH 9, the RbCl titration curve was slightly shallower than the other curves. At 0.06 and 0.3 m ionic strength and above the pH_{znpc}, the slopes of the titration curves vary with the cation, broadly screening is enhanced in the order $Li^+ > Na^+ > K^+ > Rb^+$. For the KCl data, there was a slight shift (0.1–0.2 pH units) in the pH_{znpc} values towards lower pH values. In contrast to the cations, at 0.03 and 0.3 m ionic strength, the titration curves in NaTr media were shallower than in NaCl media below the pH_{znpc}, indicating greater screening by the smaller Cl^- ion. We observed the same trends between the five electrolytes for all particle sizes.

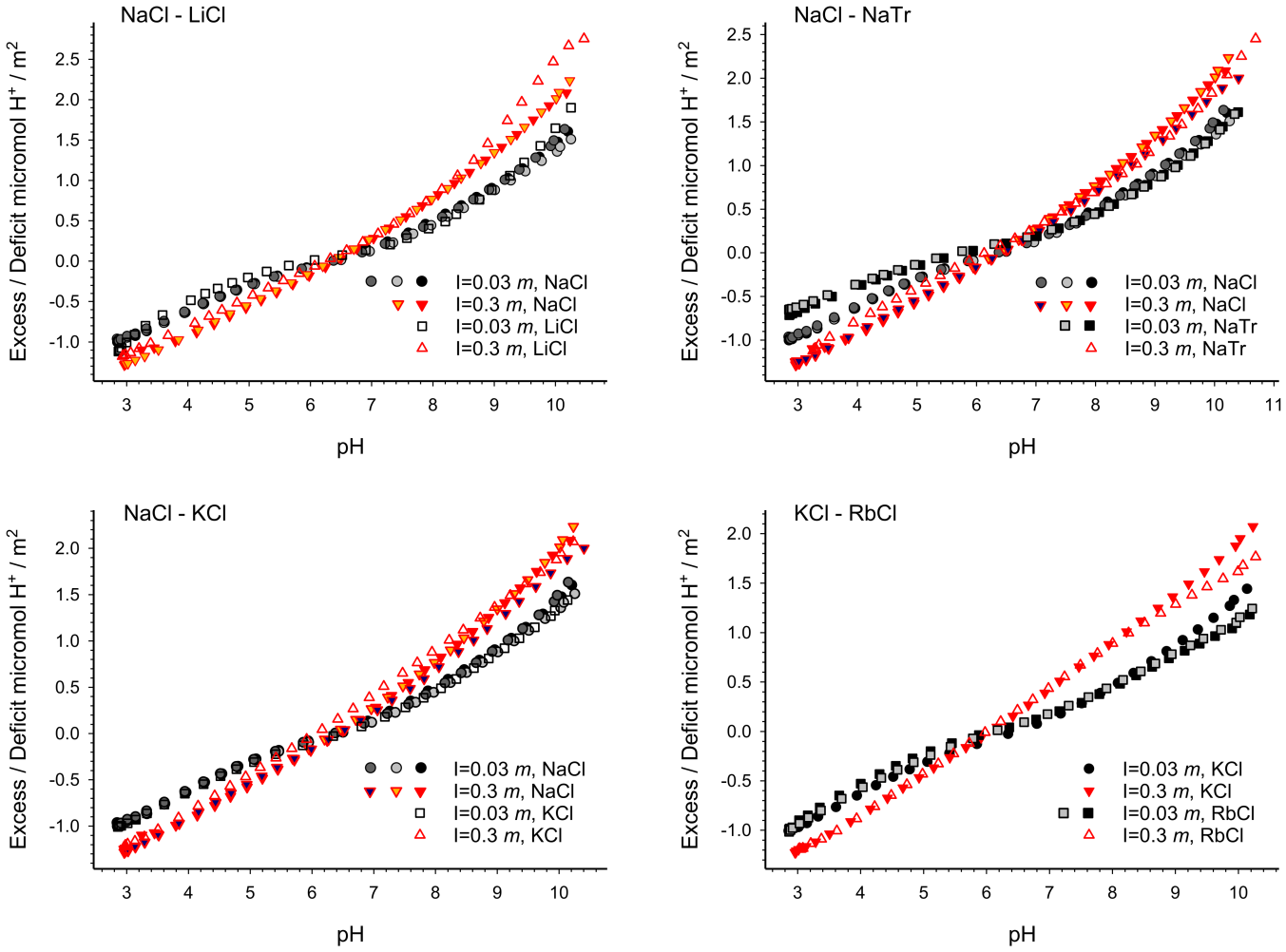

Figure 3. Relative proton adsorption or desorption on the 4 nm sized anatase sample showing the effect of electrolyte media.

3.2. Density Functional Theory Calculations

Our DFT calculations revealed only outer-sphere adsorption of Cl^- ions on the anatase (101) surface (Figure 4). In contrast, the cations adsorbed as inner-sphere complexes. The most favorable coordination environment for the cations varied relative to bare cation radii (Figure 4). The smallest ion, Li^+, formed an inner-sphere bidentate surface species to two terminal oxygen surface sites. The Na^+ ions also formed a bidentate inner-sphere complex, but with two bridging oxygen surface sites. The large K^+ and Rb^+ ions formed tetradentate surface complexes, comprising two bridging and two terminal oxygen surface sites. The

terminal oxygen atoms of the Rb^+ complex were also protonated. These inner-sphere complexes are represented by

$$2\left(\equiv \mathrm{TiOH}^{-0.3}\right) + \mathrm{Li}^+ \rightleftharpoons \left(\equiv \mathrm{TiOH}^{-0.3}\right)_2 - \mathrm{Li}^+ \quad (3)$$

$$2\left(\equiv \mathrm{Ti_2O}^{-0.7}\right) + \mathrm{Na}^+ \rightleftharpoons \left(\equiv \mathrm{Ti_2O}^{-0.7}\right)_2 - \mathrm{Na}^+ \quad (4)$$

$$2\left(\equiv \mathrm{TiOH}^{-0.3}\right) + 2\left(\equiv \mathrm{Ti_2O}^{-0.7}\right) + \mathrm{K}^+ \rightleftharpoons \left(\equiv \mathrm{TiOH}^{-0.3}\right)_2\left(\equiv \mathrm{Ti_2O}^{-0.7}\right)_2 - \mathrm{K}^+ \quad (5)$$

and

$$2\left(\equiv \mathrm{TiOH}^{-0.3}\right) + 2\left(\equiv \mathrm{Ti_2O}^{-0.7}\right) + \mathrm{Rb}^+ + 2\mathrm{H}^+ \rightleftharpoons \left(\equiv \mathrm{TiOH_2}^{+0.7}\right)_2\left(\equiv \mathrm{Ti_2O}^{-0.7}\right)_2 - \mathrm{Rb}^+ \quad (6)$$

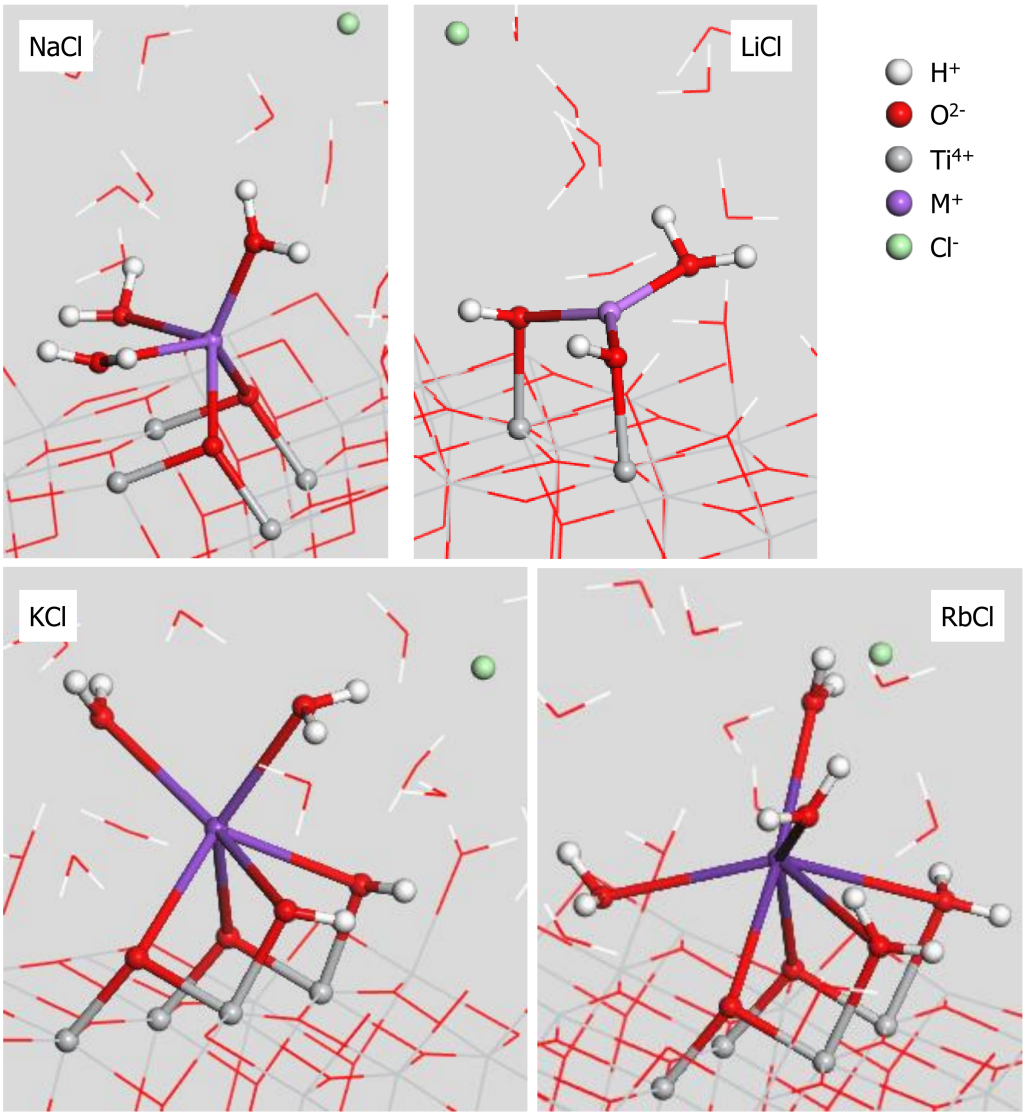

Figure 4. Schematics of the anatase (101) surface plane and representative coordination geometries for the inner-sphere (purple, M^+) bidentate Na^+ and Li^+ ions, tetradentate K^+ and Rb^+ ions, and outer-sphere (green) Cl^- ion, from the MD-DFT calculations.

The coordination geometries shown in Figure 4 are static configurations and snapshots, obtained from the MD simulations. The energy minimization results do not account for

the entropic contributions to Gibbs free energy, nor do they probe the distribution and diffusion of adsorbed ions. However, for each cation, the same optimized geometry was obtained from different starting positions.

The differences in cation adsorption geometry at the anatase surface are comparable to the cation interactions reported for the rutile (110) surface from computational studies and X-ray experiments [10,11]. The computational studies suggest that the oxygen–cation interactions play the predominant role in determining the structure of surface complexes. The large, weakly hydrated cations, such as K^+ and Rb^+, can be partially desolvated, as the oxygen atoms of the terminal and bridging surface sites substitute for the primary hydration shell. The smaller Na^+ ion, and correspondingly shorter Na^+–O bond length, likely limits the formation of Na^+ tetradentate surface species. Both Na^+ bidentate ($(\equiv Ti_2O^{-0.7})_2$–Na^+) and tetradentate inner-sphere surface complexes have been identified on rutile [11]; however, on anatase the more open structure likely makes a Na^+–tetradentate surface species less favorable. The small size of Li^+ ions, like Zn^{2+} on rutile, allows it to fit between two terminal oxygen atoms, whereas long Li^+–O bonds necessary for a tetradentate species would be unfavorable.

For each inner-sphere surface complex, the overall coordination geometry—surface ligands and primary hydration water molecules—varied with cation radii. The average coordination number (CN) for the bidentate complexes were 3 (Li^+) and 5 (Na^+), and were 6 (K^+) and 7 (Rb^+) for the tetradentate complexes. These CNs are somewhat lower than the values typically reported for the alkali ions in bulk water, although reported values depend on method and salt concentrations. Average reported coordination values are Li^+ 4; Na^+ typically 6 (5–8); K^+ 6–8; and Rb^+ 8 [46–50]. From the DFT calculations, the average alkali ion–H_2O bond lengths match the average bond lengths in bulk solution (Li^+—1.9 Å; Na^+—2.4 Å; K^+—2.8 Å; and Rb^+—3.0 Å) [49,51]. The average bond length between Li^+ and the terminal O atoms was 1.9 Å, and between Na^+ and the bridging O atoms was 2.4 Å; resulting in the primary coordination shape of the adsorbed Li^+ and Na^+ ions being symmetric. Similarly, the primary coordination geometry of K^+ was symmetric, as the four K^+ surface O atoms bonds were all ~2.8 Å. The adsorbed Rb^+ structure was somewhat distorted, as bond lengths between Rb^+ and the protonated terminal and bridging O atoms were ~3.3 Å and ~2.9 Å, respectively. The coordination shells of the adsorbed species resemble solvation shells with perturbations that arise from the different charges on the surface O atoms compared to O atoms in bulk water. The lower CNs of adsorbed cations is due to stronger alkali-surface O atom bonds, caused by the higher surface O atom electron densities [11,52]. The change from bidentate to tetradentate surface coordination is consistent with the higher charge-to-radius ratios (Z/r) in Li^+ and Na^+ compared to K^+ and Rb^+, as higher Z/r generally leads to lower CNs. Considering the optimized geometries from DFT calculations (Figure 4), it was possible to estimate the relative height of the adsorbing alkali ions above a Ti–O plane within the anatase lattice (i.e., (101) plane equivalent). The sorption positions of the Li^+ and Na^+ ions had slight lateral displacements towards the tetradentate site, rather than lying along the rows of terminal or bridging surface sites, respectively. The perpendicular adsorption height of the cations to the same Ti–O lattice plane increased in the order $Li^+ = Na^+ < K^+ < Rb^+$. Comparable results were calculated for the alkali ions above the rutile (110) surface plane [10].

3.3. Surface Complexation Modeling Framework

Our SCM efforts build on the MUSIC model description outlined in Ridley et al. [26] that described the extensive titration data set for the three anatase samples, in NaCl media. As noted above, the estimated proton affinity constants (K_H values), fractional charges of the surface functional groups, and surface Ti–O bond lengths estimated in Ridley et al. [26] were used directly in this work. The experimental data sets for each anatase sample and each electrolyte media were treated separately, giving unique fitting parameters. This approach was necessary because of the differences in slopes of the titration data, and because the protonation constants varied as a function of particle size (Table 1).

When modeling the four cation–chloride electrolyte data sets, we limited the Cl^- ion interactions with the anatase surface to outer-sphere species, as identified in our DFT simulations. We assumed that the larger Tr^- anion would also only form outer-sphere surface complexes. Interaction between the anions and anatase (101) surface was described by two monodentate species, represented by:

$$\equiv TiOH_2^{+0.7} + A^- \rightleftharpoons \equiv TiOH_2^{+0.7} \cdots A^- \quad (7)$$

$$\equiv Ti_2OH^{+0.3} + A^- \rightleftharpoons \equiv Ti_2OH^{+0.3} \cdots A^- \quad (8)$$

where A^- is either Cl^- or Tr^-.

When considering the interaction between the cations and the anatase surface, we limited the inner-sphere complexes, the predominant species, to those identified in the DFT simulations (Figure 4) and represented by Equations (3)–(6). Additionally, we tested various plausible outer-sphere coordination geometries and combinations of cation surface complexes in our fits. The best fits were achieved when two monodentate outer-sphere surface complexes were included with the predominant inner-sphere complex. The two monodentate outer-sphere cation species are represented by

$$\equiv TiOH^{-0.3} + M^+ \rightleftharpoons \equiv TiOH^{-0.3} \cdots M^+ \quad (9)$$

$$\equiv Ti_2O^{-0.7} + M^+ \rightleftharpoons \equiv Ti_2O^{-0.7} \cdots M^+ \quad (10)$$

where M^+ is Li^+, Na^+, K^+, or Rb^+.

An important consideration in SCM is the description of the electric double layer. For nanoparticles, especially particles < 10 nm in diameter, curvature of the particles leads to rapid dampening of the electric field within the EDL [20,21,53]. To account for changes in the EDL behavior as a function of size, various spherical double layer models have been applied [16,54]. Our earlier work carefully evaluated curvature effects of the EDL [25,26], and found that all titration data, in NaCl media, for the 4 nm sized particles were best described by a flat-plane model. The good fit of the flat-plane EDL model likely results from the lath-like particle morphology. Equally, Hiemstra and van Riemsdijk [21] found a flat-plane double layer model adequately described the surface charge of nanoparticle sized ferrihydrite. Consequently, in this study, the titration data for each electrolyte were described using the flat-plane EDL model. As both inner- and outer-sphere species were incorporated in our SCM, the EDL was described by inner and outer Helmholtz planes. The H^+ adsorption was limited to the surface plane. The finite charge of all outer-sphere species (both cations and anions) was located at the outer Helmholtz plane. For the inner-sphere complexes, charge was distributed between the surface and an inner-Helmholtz plane; this approach followed the charge distribution (CD) model of Hiemstra et al. [40] and van Riemsdijk and Hiemstra [55]. The CD values were calculated by considering an equal distribution of charge within the primary coordination sphere (i.e., a Pauling bond valence distribution of charge). We used the average primary hydration shell of each cation in bulk solution as a measure of the total number of ligands in the coordination sphere of the inner-sphere surface complexes. When fitting the data, some small adjustments to the CD values resulted in improved fits.

As SCMs are inherently ambiguous, we performed a variety of modeling approaches (e.g., various EDL descriptions and binding configurations). Initially, when fitting the KCl, RbCl, and LiCl data, we included potential Na^+ surface species. Similarly, Cl^- surface species were included in the NaTr fits. By including potential Na^+ and Cl^- surface species in the fits, the small contribution of Na^+ and Cl^- ions from the NaOH and HCl, respectively, were accounted for. This approach introduced a significant number of additional model parameters. Another fitting approach combined the Na^+ ions with the predominant cation and the Cl^- ions with the Tr^- anion. Although this is a somewhat simpler approach, it minimized the number of fitting parameters and consequent parameter covariance, and reduced model ambiguity. Most significantly, this approach resulted in the best model fits,

as indicated by the highest MSC values. The appropriateness for selecting this model is discussed below (see Section 4).

Table 2 lists the final set of SCM optimized parameters (including equilibrium constants, CD, capacitance, and MSC values), and Figures 1 and 2 show representative SCM fits. The modeling results presented in Table 2 for the NaCl media are different from those present in Ridley et al. [26], which used the Basic Stern layer description for the EDL. In the Supplementary Material, Table S1 lists the SCM fitting parameters relative to particle size of the three anatase samples.

Table 2. Fitting parameters for the SCM for each anatase sample, in each electrolyte media. The particle sizes are in nm, capacitance values are in units of farad per m^2; also included are the MSC values [1].

Electrolyte Media	Particle Size	C_1	Inner-sphere log K	Inner-Sphere Complex	CD	C_2	Outer-Sphere log $K \equiv \mathrm{TiOH}^{-0.3} \cdots \mathrm{M}^+$	Outer-Sphere log $K \equiv \mathrm{Ti_2O}^{-0.7} \cdots \mathrm{M}^+$	Outer-sphere log $K \equiv \mathrm{TiOH_2}^{+0.7} \cdots \mathrm{A}^-$	Outer-Sphere log $K \equiv \mathrm{Ti_2OH}^{+0.3} \cdots \mathrm{A}^-$	C_S	MSC
LiCl	4	0.9 ± 0.2	−0.5 ± 0.6	Bidentate, terminal	0.46 ± 0.71	3.9 ± 4.6	−2.0	−0.31 ± 0.21	−1.8	−0.4 ± 0.2	0.73	5.15
LiCl	20	1.2 ± 0.2	−0.45 ± 0.6	Bidentate, terminal	0.46 ± 0.64	3.0 ± 1.5	−2.0	−0.31 ± 0.25	−1.8	−0.5 ± 0.3	0.86	6.17
LiCl	40	1.5 ± 0.3	−0.5 ± 0.7	Bidentate, terminal	0.50 ± 0.66	3.0 ± 1.4	−2.0	−1.50 ± 1.86	−1.8	−0.2 ± 0.2	1.00	5.19
NaCl	4	0.9 ± 0.2	−1.3 ± 0.7	Bidentate, bridged	0.36 ± 0.59	3.9 ± 3.3	−2.0	−0.11 ± 0.08	−1.8	−0.2 ± 0.09	0.73	4.10
NaCl	20	1.1 ± 0.1	−1.3 ± 0.4	Bidentate, bridged	0.36 ± 0.26	3.9 ± 1.2	−2.0	−0.11 ± 0.07	−1.8	−0.2 ± 0.1	0.86	4.89
NaCl	40	1.3 ± 0.2	−1.3 ± 1.0	Bidentate, bridged	0.36 ± 0.63	3.9 ± 1.8	−2.0	−0.11 ± 0.13	−1.8	−0.2 ± 0.1	0.97	4.36
NaTr	4	0.9 ± 0.3	−1.3 ± 2.8	Bidentate, bridged	0.36 ± 1.9	3.9 ± 7.8	−2.0	−0.11 ± 0.26	−1.8	−1.3 ± 2.8	0.73	5.47
NaTr	20	1.1 ± 0.2	−1.3 ± 2.1	Bidentate, bridged	0.36 ± 1.3	3.9 ± 4.1	−2.0	−0.11 ± 0.28	−1.8	−0.7 ± 0.9	0.86	5.65
NaTr	40	1.2 ± 0.4	−1.3 ± 2.4	Bidentate, bridged	0.36 ± 1.4	3.9 ± 4.2	−2.0	−0.11 ± 0.31	−1.8	−0.5 ± 0.4	0.92	6.02
KCl	4	0.9 ± 0.4	−1.2 ± 2.1	Tetradentate	0.55 ± 2.7	3.9 ± 8.1	−2.0	−0.11 ± 0.12	−1.8	−0.5 ± 0.2	0.73	4.83
KCl	20	1.3 ± 0.5	−1.3 ± 2.0	Tetradentate	0.55 ± 2.3	3.9 ± 4.8	−2.0	−0.11 ± 0.10	−1.8	−0.6 ± 0.2	0.97	4.81
KCl	40	1.3 ± 0.3	−1.3 ± 1.6	Tetradentate	0.50 ± 1.8	3.9 ± 3.2	−2.0	−0.11 ± 0.08	−1.8	−0.3 ± 0.1	0.97	5.53
RbCl	4	0.9 ± 2.4	−2.1 ± 10	Tetradentate	0.50 ± 5.5	3.9 ± 45	−2.0	−0.11 ± 0.17	−1.8	−0.5 ± 0.2	0.73	5.37
RbCl	20	1.1 ± 3.0	−1.8 ± 7.8	Tetradentate	0.50 ± 3.3	3.9 ± 38	−2.0	−0.11 ± 0.24	−1.8	−0.5 ± 0.3	0.86	5.21
RbCl	40	1.1 ± 1.7	−1.8 ± 4.6	Tetradentate	0.50 ± 1.8	3.9 ± 21	−2.0	−0.11 ± 0.16	−1.8	−0.1 ± 0.1	0.86	5.14

[1] All log K values reflect infinite dilution. There are no error estimates for the outer-sphere log $K \equiv \mathrm{TiOH}^{-0.3} \cdots \mathrm{M}^+$ and log $K \equiv \mathrm{TiOH_2}^{+0.7} \cdots \mathrm{A}^-$ values because they were held constant for all data fitting.

3.4. Constrained Surface Complexation Modeling

Although the data sets for each of the three anatase samples in each electrolyte media were treated separately, fitting was performed in an iterative fashion to ensure maximum consistency between the fitting parameters (i.e., multiple fitting cycles were completed for each data set; the results from one iteration were used to refine and constrain the fitting parameters of the next cycle). For example, the outer-sphere adsorption constants for all cations to $\equiv\mathrm{TiOH}^{-0.3}$ surface sites are constant for all data sets (Table 2). Except for data in LiCl media, outer-sphere adsorption constants for cations to $\equiv\mathrm{Ti_2O}^{-0.7}$ and anions to $\equiv\mathrm{TiOH_2}^{+0.7}$ surface sites, and outer Helmholtz layer capacitance values (C_2) are constant. Capacitance values for the inner Helmholtz layer (C_1) and consequently the Stern layer capacitance (C_S, where $C_s = \frac{1}{(1/C_1)+(1/C_2)}$) varied with particle size: the values increased with increasing particle size and accounted for the steepening in slope of the titration curves (Figure 2). Stern layer capacitance values are a general characteristic of the interface domain, determined by the average distance of approach of adsorbed complexes [15]. For the nanoparticles, the C_S values may be interpreted as ions approaching the surface of the larger anatase particles more closely [26]. The C_S values vary from 0.7 to 1.0, which according to the hypothesis advanced by Bourikas et al. [30] suggests well crystallized solids; which matches the ACEM images of the samples [26]. Moreover, the average C_S values increase with increasing particle size, a trend that was not apparent from the studies summarized by Bourikas et al. [30].

Fitting parameters varied for binding constants of the predominant adsorption species, the inner-sphere cation and outer-sphere $\equiv Ti_2OH^{+0.3}\cdots A^-$ surface complexes. The binding constants for the adsorption of Cl^- ions to $\equiv Ti_2OH^{+0.3}$ surface sites ($\equiv Ti_2OH^{+0.3}\cdots Cl^-$) were stronger than the corresponding constants for Tr^- ions ($\equiv Ti_2OH^{+0.3}\cdots Tr^-$). The difference between Cl^- and Tr^- binding constants accounts for the steeper titration curve slopes, below the pH_{znpc} values, in NaCl than NaTr media. Of all fitting parameters, the binding constant for outer-sphere $\equiv Ti_2OH^{+0.3}\cdots A^-$ surface complexes were most variable, although there was a slight correlation with the inner Helmholtz layer (C_1) capacitance values.

For the inner-sphere surface complexes (Table 2), the adsorption constants decrease in the order $Li^+ > Na^+ = K^+ > Rb^+$. The Li^+ and Na^+ ions both form inner-sphere bidentate complexes, but the fitted adsorption constants and CD values for the Li^+ ions are higher than those of Na^+. The difference in fitting parameters for the adsorption of Li^+ versus Na^+ ions reflect the steeper titration curves at pH values above the pH_{znpc}, in LiCl media. Additionally, the Li-bidentate surface complex comprises two terminal surface sites, whereas Na^+ binds to two bridged surface sites (Equations (3) and (4), respectively), and the difference in CD values correspond to a lower average primary hydration number for Li^+ relative to Na^+ ions (4 versus 6, respectively). The inner-sphere adsorption constants for Na^+ and K^+ are the same, although the surface complexes have bidentate and tetradentate coordination, respectively. The difference in coordination geometry is apparent from the higher CD value for K^+ (0.55 bond valence units) than for Na^+ (0.33 bond valence units) ions. The larger CD values for K^+ correspond to a greater contribution of charge to the anatase surface layer; and may account for the slight shift in the apparent pH_{zpnc} value towards lower pH values. Fitted CD values also reflected the difference between the primary hydration numbers and inner-sphere coordination geometry of the adsorbed ions; however, fitted CD values were negatively correlated with the corresponding adsorption constants, which adds model ambiguity.

Both K^+ and Rb^+ formed tetradentate inner-sphere surface complexes (Equations (5) and (6)), but binding constants and CD values for K^+ are larger than those of Rb^+. The difference in CD values corresponds to different average primary hydration numbers of 7 and 8 for K^+ and Rb^+ ions, respectively. The stronger K^+ binding constant reflects the steeper titration curve in KCl than in RbCl media.

4. Discussion

Application of the Surface Complexation Modeling

We used the fitting parameters listed in Tables 1 and 2 to examine changes in speciation as a function of particle size, electrolyte media, and solution composition (including pH and ionic strength). Figures 5–7 and S2 show representative speciation diagrams, with all data presented as fractions of the total concentration of surface sites on the (101) anatase surface (i.e., N_S of 10.34 sites/nm^2 = 17.17 μmol/m^2). The fraction of surface sites associated with the $\equiv TiOH^{-0.3}\cdots M^+$ and $\equiv TiOH_2{}^{+0.7}\cdots A^-$ species was small, reflecting their small log *K* values; therefore, they are not shown in Figures 5–7. Except at high pH (> 9), uncomplexed species predominate (Figure 5). The dominant positive and negative surface sites were $\equiv TiOH_2{}^{+0.7}$ and $\equiv Ti_2O^{-0.7}$, respectively, which reflect their protonation constant values. At low pH, speciation of the uncomplexed surface sites is comparable in all electrolyte media. The dominant electrolyte surface complex, at low pH, is the outer-sphere $\equiv Ti_2OH^{+0.3}\cdots Cl^-$ species, with less surface coverage by the weaker $\equiv Ti_2OH^{+0.3}\cdots Tr^-$ species; these species decrease as pH increases. With increasing pH, speciation of the uncomplexed surface species vary as a function of ionic media, which can be explained by the different coordination geometry and binding strength of the inner-sphere cation surface species.

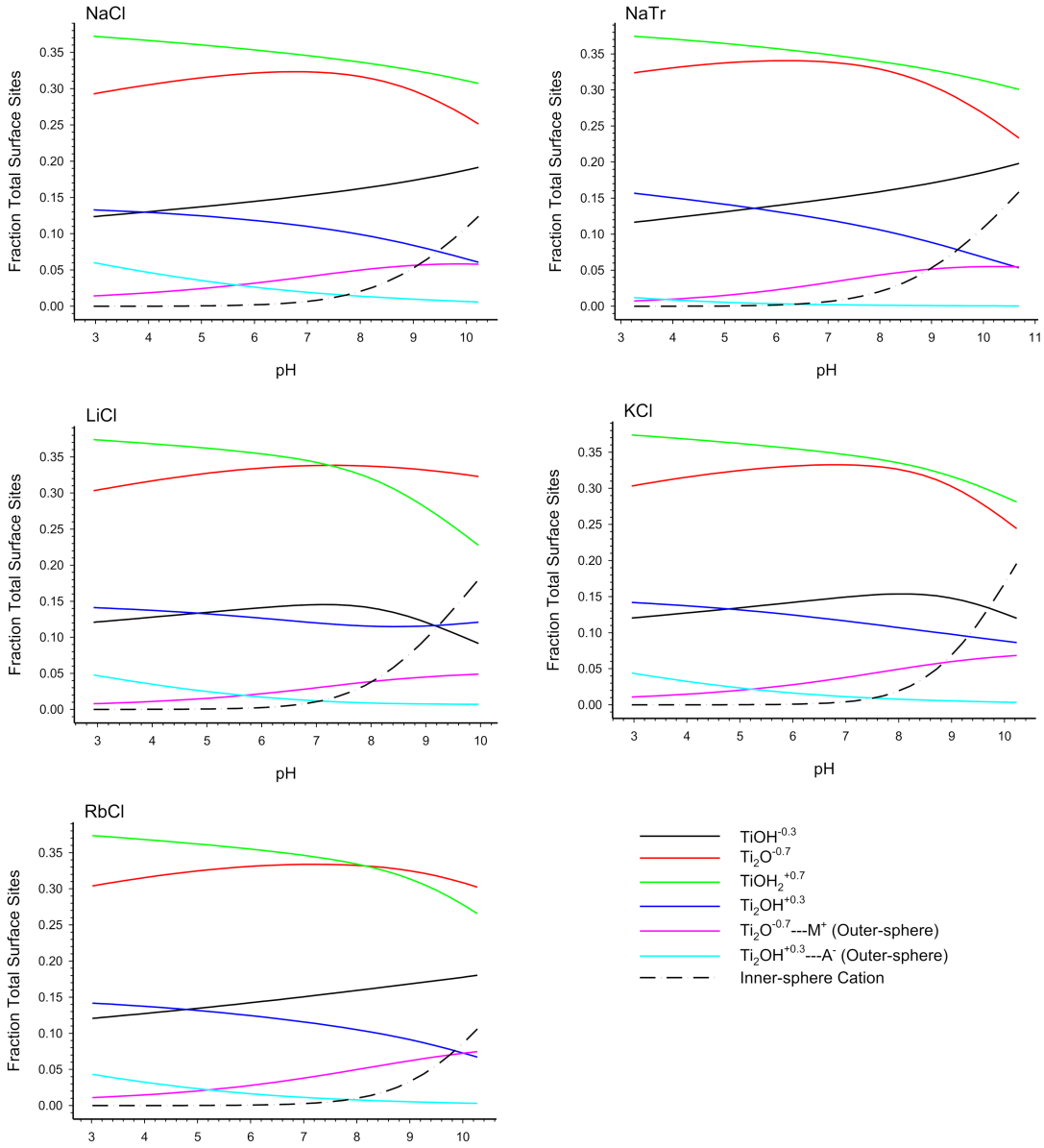

Figure 5. Distribution of surface species on the 4 nm sized anatase sample, at 0.3 m ionic strength. The inner-sphere species are described in the text.

In NaCl and NaTr media the fraction of $\equiv Ti_2O^{-0.7}$ and $\equiv Ti_2OH^{+\,0.3}$ surface sites decrease as pH increases, corresponding to the increase in the fraction of total surface sites associated with the inner-sphere bidentate $(\equiv Ti_2O^{-0.7})_2$–Na^+ species. Above pH 9, the predominant Na^+ surface complex shifts from outer-sphere to the inner-sphere $(\equiv Ti_2O^{-0.7})_2$–Na^+. The speciation results are different in LiCl media; with the fraction of $\equiv TiOH_2^{+0.7}$ and $\equiv TiOH^{-0.3}$ species decreasing as the inner-sphere bidentate $(\equiv TiOH^{-0.3})_2$–Li^+ species increases. The inner-sphere Li^+ surface complex predominates over the outer-sphere above pH 8. In KCl media, all uncomplexed surface species decrease with increasing pH, corresponding to the formation of the inner-sphere tetradentate $(\equiv TiOH^{-0.3})_2(\equiv Ti_2O^{-0.7})_2$–$K^+$ surface complex. In contrast, only the $\equiv Ti_2O^{-0.7}$, $\equiv TiOH_2^{+0.7}$, and $\equiv Ti_2OH^{+0.3}$ species decrease with the formation of the weaker inner-sphere tetradentate $(\equiv TiOH_2^{+0.7})_2(\equiv Ti_2O^{-0.7})_2$–$Rb^+$ complex.

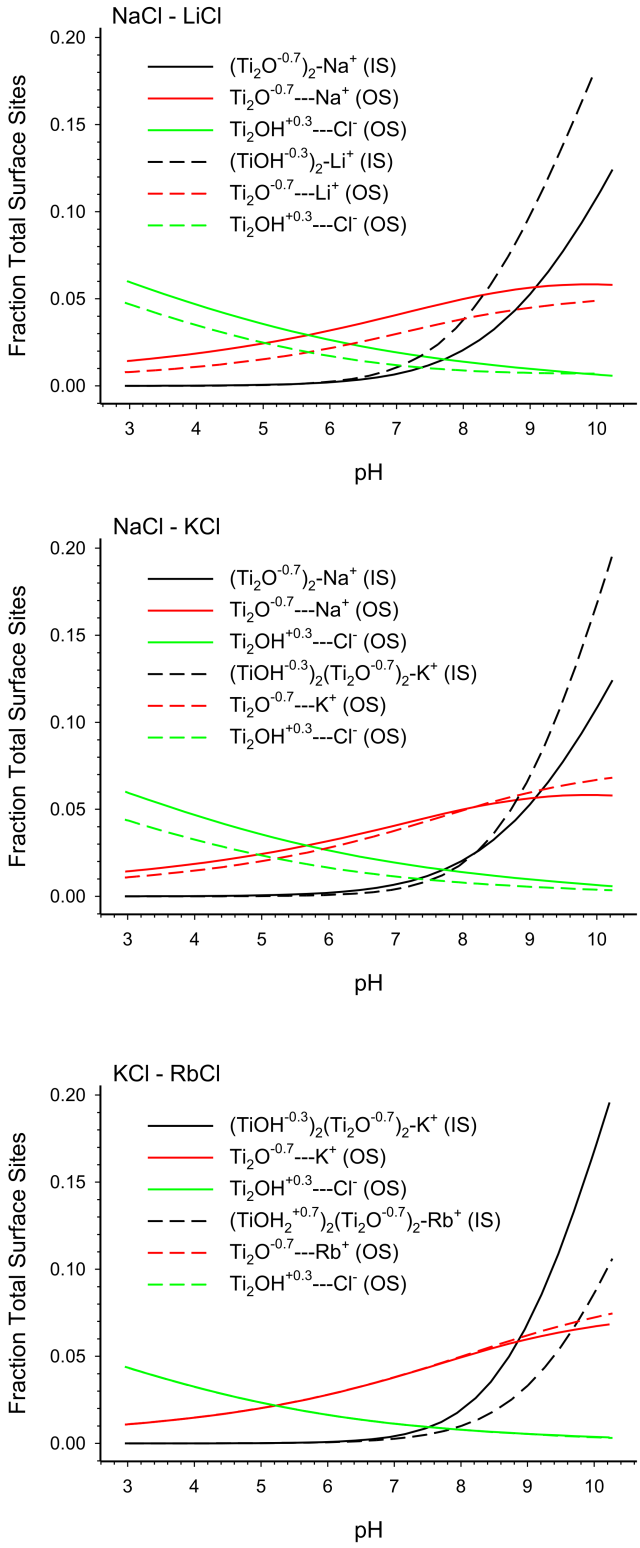

Figure 6. Distribution of surface species on the 4 nm sized anatase sample showing the effect of electrolyte media, at 0.3 m ionic strength. The plots show the inner-sphere (IS) and predominant outer-sphere (OS) electrolyte surface species.

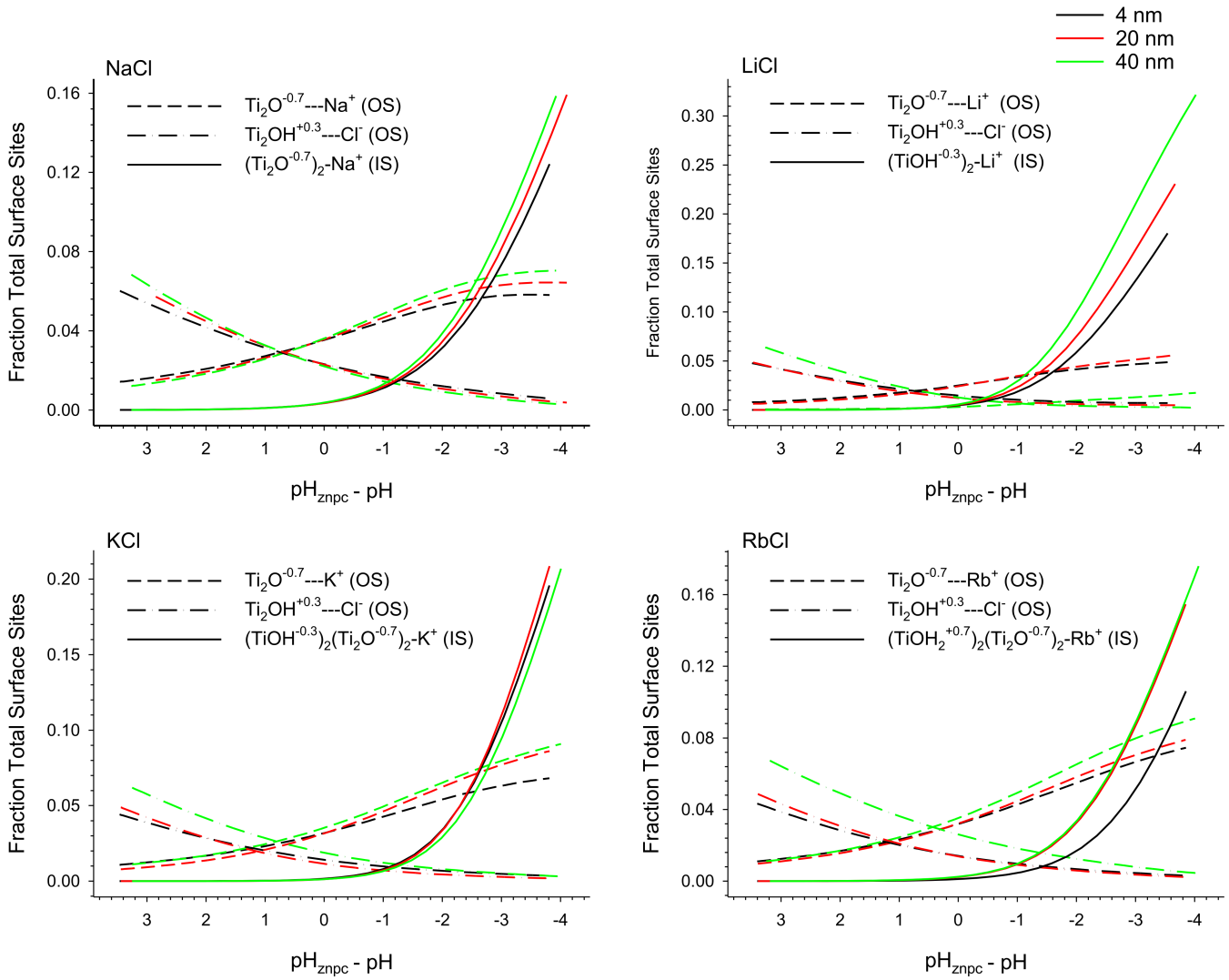

Figure 7. Effect of particle size on the distribution of surface species, as a function of pH_{znpc}-pH. The black, red, and green lines represent particle sizes of 4, 20, and 40 nm, respectively. Data are presented for the inner-sphere and predominant outer-sphere electrolyte surface species, at 0.3 m ionic strength.

Figure 6 shows the effects of ionic media on surface speciation, specifically for the inner-sphere species bi- and tetradentate complexes. The stronger bidentate Li^+ complex ($(\equiv TiOH^{-0.3})_2$–Li^+) dominates at lower pH than the Na^+ complex ($(\equiv Ti_2O^{-0.7})_2$–Na^+). As the strength of the inner-sphere Na^+ and K^+ binding constants are similar, the tetradentate $(\equiv TiOH^{-0.3})_2(\equiv Ti_2O^{-0.7})_2$–$K^+$ surface complex is associated with a greater fraction of surface sites. Although the coordination geometry of the tetradentate K^+ and Rb^+ complexes are the same (except for the protonation state of the terminal site), the stronger binding constant for the K^+ species is reflected by the greater fraction of associated surface sites and the lower pH values at which the inner-sphere complex becomes dominant.

In all cation-Cl electrolyte media, the total fraction of surface sites associated with the cations is quite low, even for the inner-sphere tetradentate K^+ and Rb^+ complexes (Figures 5 and 6). Similarly, the fraction of surface sites associated with the Tr^- ion is low. The relatively small fraction of surface sites associated with the electrolyte ions contributed to our choice of modeling approach (see Section 3.3); of combining the Na^+ ions with the predominant cation (i.e., in KCl, RbCl, and LiCl media), and combing Cl^- with the Tr^- ions in NaTr media. In all cases, if the models had considered the contribution of Na^+ and Cl^- ions separately, the fractions of surface sites associated with either Na^+ or Cl^- would have been less than 1.5% (i.e., confidence in such low coverage would be minimal).

To directly evaluate particle size effects on surface site speciation, Figure 7 presents data relative to the respective pH_{znpc} values of the three anatase samples in 0.3 *m* media. In NaCl and LiCl media (and NaTr media, not shown), the fraction of surface sites associated with the dominant electrolyte complexes increase with increasing particle size. The effect of particle size is limited in KCl media, but in RbCl media there is noticeably less association between the large Rb^+ ion and the smallest (4 nm) sized particles, which agrees with the log *K* values reported in Table 2. Similar results were observed at all ionic strengths (see Figure S2 for an example of ionic strengths effects in NaCl media).

5. Conclusions

The present study advances our understanding of nanoparticle anatase–water interfaces in two important respects. First, trends observed in the charging behavior of three monodispersed nanometer size anatase samples in NaCl media [26] extend to other 1:1 electrolyte media. Specifically, the slope of surface charging curves increased with increasing particle size both above and below the pH_{znpc} values in NaCl, NaTr, LiCl, KCl, and RbCl media. Secondly, the surface charging behavior of the different sized nanoparticle anatase powders all followed a reverse monovalent cation lyotropic series. Furthermore, the average Stern layer capacitance values (C_S) increase with increasing particle size. As for the rutile (TiO_2) polymorph, the monovalent electrolyte cations adsorbed as inner-sphere complexes, and as suggested by our MD-DFT results, the coordination geometry and structure of the interfacial domain are controlled by the size and desolvation of the inner-sphere cations.

Supplementary Materials: The following supporting information can be downloaded at https://www.mdpi.com/article/10.3390/min12070907/s1, Table S1: Fitting parameters for the SCM for each anatase sample, in each electrolyte media. The particle diameters are in nm, capacitance values are in units of farad per m^2, also included are the MSC values; Figure S1: Periodic model of anatase (101) surface with Rb^+ as a bidentate surface complex following energy minimization; Figure S2: Effect of ionic strength of the distribution of surface species on the 4 nm diameter anatase sample. Data are presented for the inner-sphere and predominant outer-sphere electrolyte surface species, in NaCl media. Excel formatted experimental surface charge titration data and corresponding SCM model fits are available in Supplementary Materials.

Author Contributions: Conceptualization, M.K.R.; methodology, M.K.R., M.L.M. and J.D.K.; analysis, M.K.R. and M.L.M.; writing—original draft preparation, M.K.R.; writing—review and editing, M.K.R. and M.L.M.; project administration, M.K.R.; funding acquisition, M.K.R., M.L.M. and J.D.K. All authors have read and agreed to the published version of the manuscript.

Funding: M.K.R. acknowledges funding from the National Science Foundation (CHE-1308726 and EAR-0842526).

Data Availability Statement: All data are available in the Excel file of the Supplementary Materials.

Acknowledgments: Computational support was provided by the Penn State Institute for Cyber-Science Advanced CyberInfrastructure.

Conflicts of Interest: The authors declare no conflict interest.

References

1. Gmür, T.A.; Goel, A.; Brown, M.A. Quantifying specific ion effects on the surface potential and charge density at silica nanoparticle—Aqueous electrolyte interfaces. *J. Phys. Chem. C* **2016**, *120*, 16617–16625. [CrossRef]
2. Hiemstra, T.; Van Riemsdijk, W. Physical chemical interpretation of primary charging behaviour of metal (hydr) oxides. *Colloids Surf.* **1991**, *59*, 7–25. [CrossRef]
3. Rietra, R.P.; Hiemstra, T.; van Riemsdijk, W.H. The relationship between molecular structure and ion adsorption on variable charge minerals. *Geochim. Cosmochim. Acta* **1999**, *63*, 3009–3015. [CrossRef]
4. Dove, P.M.; Craven, C.M. Surface charge density on silica in alkali and alkaline earth chloride electrolyte solutions. *Geochim. Cosmochim. Acta* **2005**, *69*, 4963–4970. [CrossRef]
5. Allen, N.; Machesky, M.L.; Wesolowski, D.J.; Kabengi, N. Calorimetric study of alkali and alkaline-earth cation adsorption and exchange at the quartz-solution interface. *J. Colloid Interface Sci.* **2017**, *504*, 538–548. [CrossRef]

6. Pfeiffer-Laplaud, M.; Gaigeot, M.-P. Adsorption of singly charged ions at the hydroxylated (0001) α-quartz/water interface. *J. Phys. Chem. C* **2016**, *120*, 4866–4880. [CrossRef]
7. Dishon, M.; Zohar, O.; Sivan, U. From repulsion to attraction and back to repulsion: The effect of NaCl, KCl, and CsCl on the force between silica surfaces in aqueous solution. *Langmuir* **2009**, *25*, 2831–2836. [CrossRef] [PubMed]
8. Dishon, M.; Zohar, O.; Sivan, U. Effect of cation size and charge on the interaction between silica surfaces in 1:1, 2:1, and 3:1 aqueous electrolytes. *Langmuir* **2011**, *27*, 12977–12984. [CrossRef]
9. Flores, S.C.; Kherb, J.; Konelick, N.; Chen, X.; Cremer, P.S. The effects of hofmeister cations at negatively charged hydrophilic surfaces. *J. Phys. Chem. C* **2012**, *116*, 5730–5734. [CrossRef]
10. Zhang, Z.; Fenter, P.; Cheng, L.; Sturchio, N.C.; Bedzyk, M.J.; Předota, M.; Bandura, A.; Kubicki, J.D.; Lvov, S.N.; Cummings, P.T.; et al. Ion adsorption at the rutile-water interface: Linking molecular and macroscopic properties. *Langmuir* **2004**, *20*, 4954–4969. [CrossRef]
11. Předota, M.; Zhang, Z.; Fenter, P.; Wesolowski, D.J.; Cummings, P.T. Electric double layer at the rutile (110) surface. 2. adsorption of ions from molecular dynamics and X-ray experiments. *J. Phys. Chem. B* **2004**, *108*, 12061–12072. [CrossRef]
12. Hawkins, T.; Allen, N.; Machesky, M.L.; Wesolowski, D.J.; Kabengi, N. Ion exchange thermodynamics at the rutile-water interface: Flow microcalorimetric measurements and surface complexation modeling of Na–K–Rb–Cl–NO_3 adsorption. *Langmuir* **2017**, *33*, 4934–4941. [CrossRef] [PubMed]
13. Lützenkirchen, J. Specific ion effects at two single-crystal planes of sapphire. *Langmuir* **2013**, *29*, 7726–7734. [CrossRef] [PubMed]
14. Sverjensky, D.A. Prediction of surface charge on oxides in salt solutions: Revisions for 1:1 (M^+L^-) electrolytes. *Geochim. Cosmochim. Acta* **2005**, *69*, 225–257. [CrossRef]
15. Ridley, M.K.; Hiemstra, T.; van Riemsdijk, W.H.; Machesky, M.L. Inner-sphere complexation of cations at the rutile-water interface: A concise surface structural interpretation with the CD and MUSIC model. *Geochim. Cosmochim. Acta* **2009**, *73*, 1841–1856. [CrossRef]
16. Abbas, Z.; Labbez, C.; Nordholm, S.; Ahlberg, E. Size-dependent surface charging of nanoparticles. *J. Phys. Chem. C* **2008**, *112*, 5715–5723. [CrossRef]
17. Barnard, A.; Zapol, P. A model for the phase stability of arbitrary nanoparticles as a function of size and shape. *J. Chem. Phys.* **2004**, *121*, 4276–4283. [CrossRef]
18. Engates, K.E.; Shipley, H.J. Adsorption of Pb, Cd, Cu, Zn, and Ni to titanium dioxide nanoparticles: Effect of particle size, solid concentration, and exhaustion. *Environ. Sci. Pollut. Res.* **2010**, *18*, 386–395. [CrossRef]
19. Gribb, A.A.; Banfield, J.F. Particle size effects on transformation kinetics and phase stability in nanocrystalline TiO_2. *Am. Mineral.* **1997**, *82*, 717–728. [CrossRef]
20. Vayssieres, L. On the effect of nanoparticle size on water-oxide interfacial chemistry. *J. Phys. Chem. C* **2009**, *113*, 4733–4736. [CrossRef]
21. Hiemstra, T.; Van Riemsdijk, W.H. A surface structural model for ferrihydrite I: Sites related to primary charge, molar mass, and mass density. *Geochim. Cosmochim. Acta* **2009**, *73*, 4423–4436. [CrossRef]
22. Suttiponparnit, K.; Jiang, J.; Sahu, M.; Suvachittanont, S.; Charinpanitkul, T.; Biswas, P. Role of surface area, primary particle size, and crystal phase on titanium dioxide nanoparticle dispersion properties. *Nanoscale Res. Lett.* **2010**, *6*, 27. [CrossRef] [PubMed]
23. Zhou, D.; Ji, Z.; Jiang, X.; Dunphy, D.R.; Brinker, J.; Keller, A.A. Influence of material properties on TiO2 nanoparticle agglomeration. *PLoS ONE* **2013**, *8*, e81239. [CrossRef]
24. Ridley, M.K.; Hackley, V.A.; Machesky, M.L. Characterization and surface-reactivity of nanocrystalline anatase in aqueous solutions. *Langmuir* **2006**, *22*, 10972–10982. [CrossRef] [PubMed]
25. Ridley, M.K.; Machesky, M.L.; Kubicki, J.D. A comparison of the reactivity at the solid-solution interface of nano- and microcrystalline TiO_2 phases. In Proceedings of the Goldschmidt Conference, Prague, Czech Republic, 14–19 August 2011.
26. Ridley, M.K.; Machesky, M.L.; Kubicki, J.D. Anatase nanoparticle surface reactivity in NaCl media: A CD–MUSIC model interpretation of combined experimental and DFT studies. *Langmuir* **2013**, *29*, 8572–8583. [CrossRef]
27. Ridley, M.K.; Machesky, M.L.; Kubicki, J.D. Experimental study of strontium adsorption on anatase nanoparticles as a function of size with a density functional theory and CD model interpretation. *Langmuir* **2014**, *31*, 703–713. [CrossRef] [PubMed]
28. Levine, S.; Neale, G.H. The prediction of electrokinetic phenomena within multiparticle systems. I. Electrophoresis and electroosmosis. *J. Colloid Interface Sci.* **1974**, *47*, 520–529. [CrossRef]
29. Sprycha, R. Surface charge and adsorption of background electrolyte ions at anatase/electrolyte interface. *J. Colloid Interface Sci.* **1984**, *102*, 173–185. [CrossRef]
30. Bourikas, K.; Hiemstra, T.; Van Riemsdijk, W.H. Ion pair formation and primary charging behaviour of titanium oxide (anatase and rutile). *Langmuir* **2001**, *17*, 749–756. [CrossRef]
31. Schmidt, J.; Vogelsberger, W. Aqueous long-term solubility of titania nanoparticles and titanium(IV) hydrolysis in a sodium chloride system studied by adsorptive stripping voltammetry. *J. Solut. Chem.* **2009**, *38*, 1267–1282. [CrossRef]
32. Shkol'Nikov, E.V. Thermodynamics of the dissolution of amorphous and polymorphic TiO2 modifications in acid and alkaline media. *Russ. J. Phys. Chem. A* **2016**, *90*, 567–571. [CrossRef]
33. Dickson, A.; Wesolowski, D.; Palmer, D.A.; Mesmer, R. Dissociation Constant of Bisulfate Ion in Aqueous Sodium Chloride Solutions to 250 °C. *J. Phys. Chem.* **1990**, *94*, 7978–7985. [CrossRef]

34. Kresse, G.; Furthmüller, J. Efficient iterative schemes for ab initio total-energy calculations using a plane-wave basis set. *Phys. Rev. B* **1996**, *54*, 11169–11186. [CrossRef] [PubMed]
35. Kresse, G.; Hafner, J. Ab initio molecular dynamics for open-shell transition metals. *Phys. Rev. B* **1993**, *48*, 13115–13118. [CrossRef]
36. Nosé, S. A unified formulation of the constant temperature molecular dynamics methods. *J. Chem. Phys.* **1984**, *81*, 511–519. [CrossRef]
37. Nosé, S. A molecular dynamics method for simulations in the canonical ensemble. *Mol. Phys.* **2002**, *100*, 191–198. [CrossRef]
38. Shock, E.L.; Koretsky, C.M. Metal-organic complexes in geochemical processes: Calculation of standard partial molal thermodynamic properties of aqueous acetate complexes at high pressures and temperatures. *Geochim. Cosmochim. Acta* **1993**, *57*, 4899–4922. [CrossRef]
39. ICSD. *Inorganic Crystal Structure Database*; Fiz, F., Ed.; GmbH: Karlsruhe, Germany, 2005.
40. Hiemstra, T.; Venema, P.; van Riemsdijk, W. Intrinsic proton affinity of reactive surface groups of metal (hydr) oxides: The bond valence principle. *J. Colloid Interface Sci.* **1996**, *184*, 680–692. [CrossRef]
41. Machesky, M.L.; Wesolowski, D.J.; Palmer, D.A.; Ridley, M.K. On the temperature dependence of intrinsic surface protonation equilibrium constants: An extension of the revised MUSIC model. *J. Colloid Interface Sci.* **2001**, *239*, 314–327. [CrossRef]
42. Barnard, A.S.; Zapol, P. Effects of particle morphology and surface hydrogenation on the phase stability of TiO_2. *Phys. Rev. B* **2004**, *70*, 235403. [CrossRef]
43. Lazzeri, M.; Vittadini, A.; Selloni, A. Structure and energetics of stoichiometric TiO_2 anatase surfaces. *Phys. Rev. B* **2001**, *63*, 155409. [CrossRef]
44. Hummer, D.R.; Kubicki, J.D.; Kent, P.R.C.; Post, J.E.; Heaney, P.J. Origin of nanoscale phase stability reversals in titanium oxide polymorphs. *J. Phys. Chem. C* **2009**, *113*, 4240–4245. [CrossRef]
45. Akaike, H. An information criterion (AIC). *Math. Sci.* **1976**, *14*, 5–9.
46. Ikeda, T.; Boero, M.; Terakura, K. Hydration of alkali ions from first principles molecular dynamics revisited. *J. Chem. Phys.* **2007**, *126*, 034501. [CrossRef]
47. Marcus, Y. Ionic radii in aqueous solutions. *Chem. Rev.* **1988**, *88*, 1475–1498. [CrossRef]
48. Varma, S.; Rempe, S.B. Coordination numbers of alkali metal ions in aqueous solutions. *Biophys. Chem.* **2006**, *124*, 192–199. [CrossRef]
49. Mähler, J.; Persson, I. A study of the hydration of the alkali metal ions in aqueous solution. *Inorg. Chem.* **2011**, *51*, 425–438. [CrossRef]
50. Tunell, I.; Lim, C. Factors governing the metal coordination number in isolated group IA and IIA metal hydrates. *Inorg. Chem.* **2006**, *45*, 4811–4819. [CrossRef]
51. Marcus, Y. *Ion Properties*; Marcel Dekker: New York, NY, USA, 1997; 259p.
52. Bandura, A.V.; Kubicki, J.D. Derivation of force field parameters for TiO_2–H_2O systems from ab initio calculations. *J. Phys. Chem. B* **2003**, *107*, 11072–11081. [CrossRef]
53. Hiemstra, T.; van Riemsdijk, W.H. On the relationship between charge distribution, surface hydration, and the structure of the interface of metal hydroxides. *J. Colloid Interface Sci.* **2006**, *301*, 1–18. [CrossRef]
54. Ohshima, H.; Healy, T.W.; White, L.R. Accurate analytic expressions for the surface charge density/surface potential relationship and double-layer potential distribution for a spherical colloidal particle. *J. Colloid Interface Sci.* **1982**, *90*, 17–26. [CrossRef]
55. Van Riemsdijk, W.H.; Hiemstra, T. The CD-MUSIC model as a framework for interpreting ion adsorption on metal (hydr) oxide surfaces. In *Surface Complexation*; Luetzenkirchen, J., Ed.; Elsevier: Amsterdam, The Netherlands, 2006; Volume 11, pp. 251–268.